Himematsu and Ozawa
*Earth, Planets and Space* (2024) 76:41
https://doi.org/10.1186/s40623-024-01988-8

Earth, Planets and Space

FULL PAPER

Open Access

# Ground deformations associated with an overpressurized hydrothermal systems at Azuma volcano (Japan) revealed by InSAR data

Yuji Himematsu[1,2*] and Taku Ozawa[2]

**Abstract**

Inflations at active volcanoes are indicators of overpressure in the subsurface, which is known to be a phenomenon that precedes eruptions. Volcanic overpressure is induced by the injection of magmatic fluids, accumulated magma, or heat supply from greater depths. Azuma volcano (Japan) has experienced several episodes of volcanic unrest with increases in seismicity at the depth of the hydrothermal system, implying a potential increase in phreatic eruptions. The time series of interferometric synthetic aperture radar data, associated with the unrest episodes occurring in 2014–2015 and 2018–2019, revealed spatiotemporal variations of inflation episodes, centered around Oana crater, the most active fumarole of Azuma volcano. The modeled best-fit geometry of the elongated pressure source for the local deformation has the same dip as the overlying topographic slope direction and angle around Oana crater, suggesting the existence of topography-correlated layered structures within the hydrothermal system. In contrast, the broader deformation associated with the 2014–2015 unrest was explained by the overpressure of a horizontal flat source at 360–1500 m below sea level, showing the similar depth of the top as the conductive low-resistivity or low-viscosity body suggested by previous studies. The unrest episodes were thus interpreted as resulting mainly from the supply of magmatic fluids, or the transfer of heat from greater depths. Our study helps in understanding the shallow structure of this volcanic system and contributes to evaluating the potential for forthcoming eruptions in Azuma volcano.

**Keywords** InSAR, Hydrothermal system, Azuma volcano, Ground deformation, Overpressure, Markov chain Monte Carlo

*Correspondence:
Yuji Himematsu
hime-matsu@eri.u-tokyo.ac.jp
Full list of author information is available at the end of the article

**Graphical Abstract**

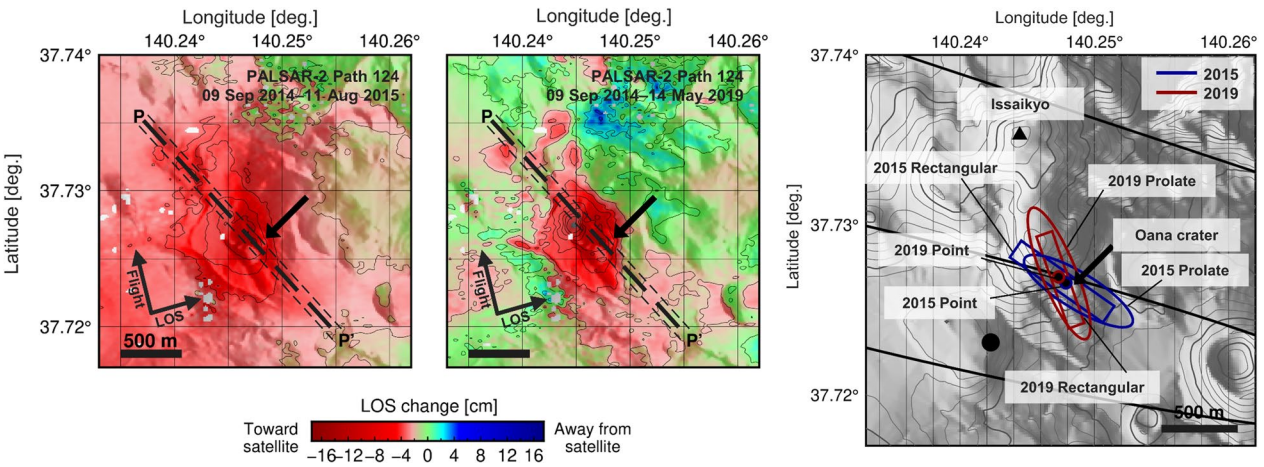


## Introduction

Evaluating pressure conditions within volcanic systems aids in understanding their potential for eruption. The overpressure in volcanic systems is induced by the accumulation of magma, or the supply of heat, or magmatic fluids from greater depths (Amelung et al. 2000; Feigl et al. 2000). These phenomena are regarded as potential precursors to volcanic eruptions and commonly induce unrests, usually accompanied by seismicity or ground deformations. For phreatic eruptions, subtle and limited precursory seismicity can be detectable (Jolly et al. 2010; Kato et al. 2015) or in some cases, it might be absent (Maeda et al. 2015). Although detecting precursory deformations prior to phreatic eruptions are generally challenging because of small amplitudes or limited spatial extent of the deformation, some studies have succeeded by using interferometric synthetic aperture radar (InSAR) data (Kobayashi et al. 2018; Narita et al. 2020). Revealing the spatial characteristics of ground deformations with a high spatial resolution better constrains the geometry of pressure sources within shallow hydrothermal systems (Hamling et al. 2016; Juncu et al. 2017; Doke

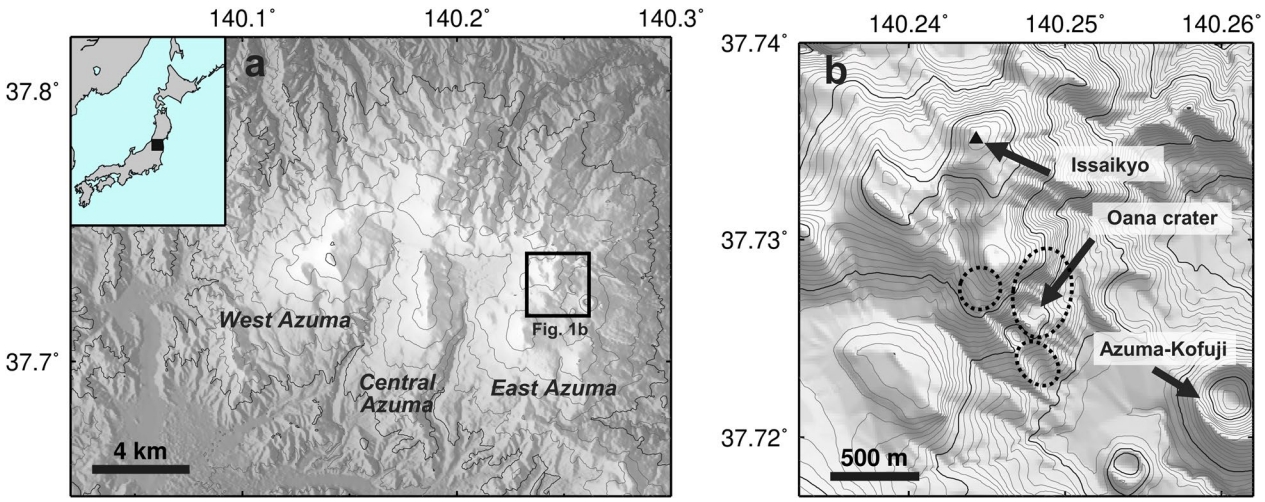


**Fig. 1** Study area map. **a** Topographic map of Azuma volcano. Thick and thin contours were set to 1000 m and 200 m intervals, respectively. **b** Enlarged topographic map of Oana crater. Thick and thin contours were set to 200 m and 20 m intervals, respectively. Dashed ellipses indicate extents of geothermal area. The background topography map was based on the 10 m grid digital elevation model released by the Geospatial Information Authority of Japan

et al. 2021; Yunjun et al. 2021). Precise monitoring of ground deformations using InSAR with high spatial resolution is essential for understanding the geometry of subsurface volcanic systems and their pressure conditions.

Azuma volcano is one of the active volcanic groups located in northeastern Japan, including West, Central, and East Azuma volcanoes (Fig. 1). Oana crater is the most active fumarole on East Azuma volcano, which is located within the northwest–southeast alignment of pyroclastic cones/craters (Yamamoto 2005). The latest eruption at Oana crater occurred in 1977 and was accompanied by tephra fall and mud ejection (Kawanabe and Ueki 2013).

Two clusters of earthquakes on Azuma volcano were identified by seismic observations (JMA 2020). The shallower cluster was distributed between 1.5 km above sea level (a.s.l.) and 0.5 km below sea level (b.s.l.) beneath Oana crater indicating volcano-tectonic earthquakes and low-frequency earthquakes associated with the unrest episodes. The deeper cluster was distributed at 20–40 km b.s.l. and approximately 5 km east of East Azuma volcano indicating regularly occurring deep low-frequency earthquakes. The extent of the deeper earthquake cluster was assumed to align with a magma reservoir that provided volcanic materials to the shallower magma storage and the hydrothermal system (Ban et al. 2016). The existence of a conductive low-resistivity structure or a low-viscosity body between the two clusters has been reported by a magnetotelluric survey (Ichiki et al. 2021) and geodetic observations (Ozawa and Fujita 2013; Takada and Fukushima 2013).

Episodes of subsidence also occurred at Azuma volcano, driven by the extension of a low viscous body beneath Azuma volcano associated with the 2011 Tohoku–Oki earthquake (Ozawa and Fujita 2013; Takada and Fukushima 2013). The volcanic subsidence induced by the 2011 earthquake was also detected at other volcanoes in the Tohoku region. The subsidence at Azuma extended from the north of East Azuma volcano to Adatara volcano, which is located approximately 12 km south of Azuma. Results from a numerical model suggested that the subsidence was induced by the extension of a long and low viscous body with a top depth of approximately 1260 m b.s.l., cause by the 2011 earthquake (Takada and Fukushima 2013). A similar subsidence at active volcanoes, associated with mega-thrust earthquakes, was also reported in Chile (Pritchard et al. 2013). There have been reports on the activation of seismic swarms in several regions of northeastern Japan due to spatiotemporal variation of pore fluid pressure triggered by the 2011 earthquake (Okada et al. 2011; Yoshida et al. 2016). However, no notable anomalous seismic activity around Azuma volcano from background level was reported.

An increase in both volcano-tectonic and low-frequency earthquakes through 2014–2015 and 2018–2019 was observed within the shallower earthquake cluster along with a GNSS baseline extension crossing over Oana crater (JMA 2020). These observations constrained the position of an isotropic inflation source at approximately 1200 m a.s.l. as the shallowest pressure source of likely hydrothermal origin (JMA 2020). An increase in the composition ratio of $SO_2/H_2S$ within a fumarole from Oana crater was reported in June 2018, implying that the volcanic volatile responsible for the inflation of this shallow source were supplied from greater depths. In contrast, the count of low-frequency earthquakes within the deeper cluster and the maximum fumarole height of Oana crater have remained consistent since the end of 2011 (JMA 2020). So far, the details of the spatiotemporal characteristics of the ground deformation and the geometry of the pressure source have been still being discussing.

In this study, we present the spatiotemporal variations of ground deformations at Azuma volcano associated with the unrest episodes in 2014–2015 and 2018–2019 using PALSAR-2 and Sentinel-1 data. Based on the detected ground deformations, we explored the geometry of the pressure sources at Azuma volcano compared them with previous models, and discussed the physical mechanisms that drive ground deformations.

## Methodology

### SAR data and analysis

We processed the L-band ALOS-2/PALSAR-2 data that were acquired during 2014–2020, and C-band Sentinel-1 data during 2017–2020 to reveal the spatiotemporal variations in ground deformation on Azuma volcano (Additional file 1: Table S1, Fig. S1). The time series of line-of-sight (LOS) changes were inferred by solving a least-squares problem using several InSAR with various temporal baselines. This process is known as the multi-temporal InSAR (MTI) analysis (Berardino et al. 2002; Schmidt and Bürgmann 2003). L-band InSAR data tend to avoid decorrelation problems even when the temporal baseline exceeds 1 year, although only 1–4 PALSAR-2 data per year were available in this case. In contrast, C-band InSAR data were strongly affected by variations in the back-scatter characteristics of the ground. Most part of Azuma volcano was covered by vegetation in summer, except for the geothermal area around Oana crater, and heavy snow during the winter. We employed Sentinel-1 data to reveal the time series of LOS changes during the periods with no snow coverage on the exposed ground around this crater. Subsets of the Sentinel-1 LOS changes were used to complement the time series of PALSAR-2 LOS changes. No temporal threshold was set

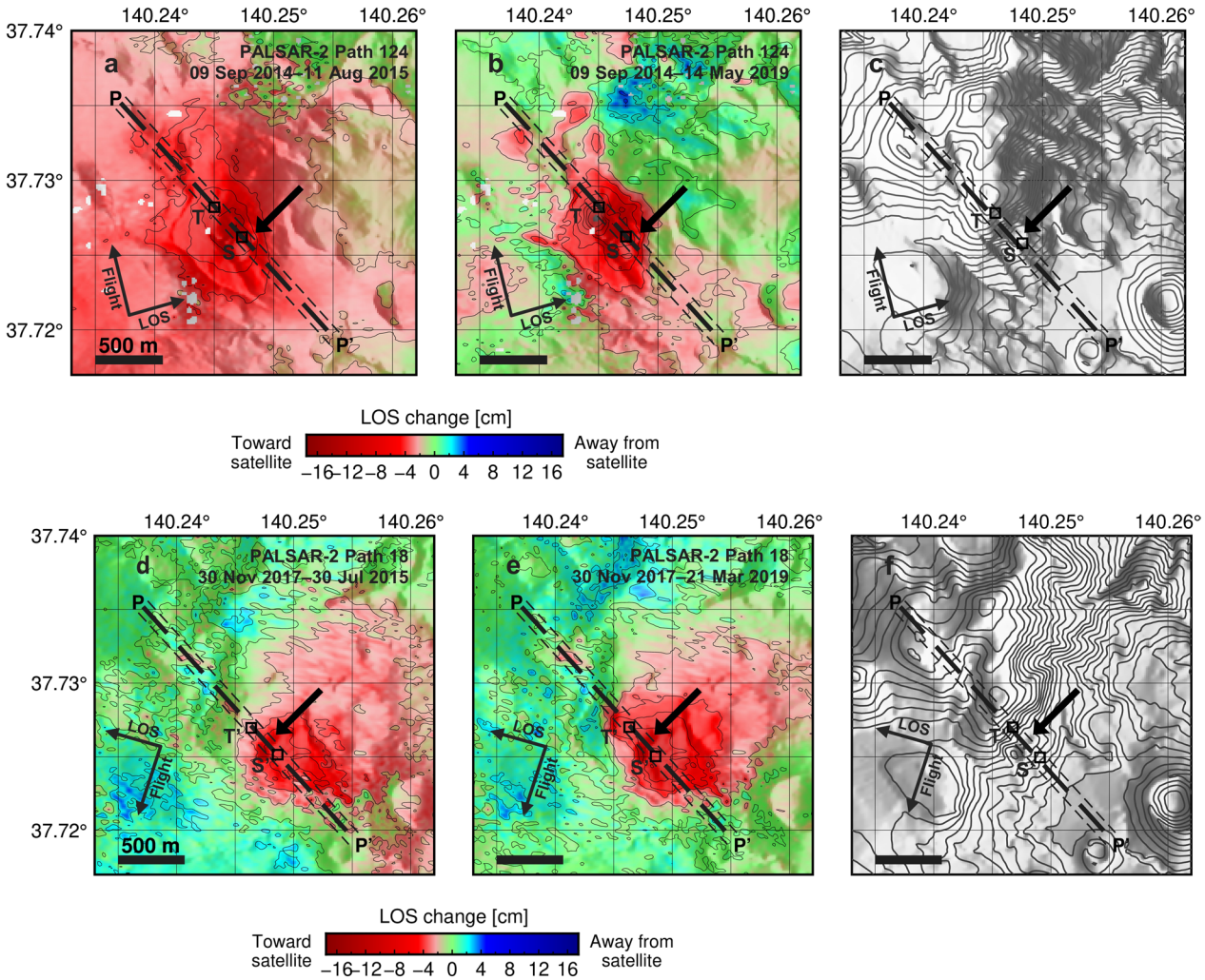


**Fig. 2** Cumulative PALSAR-2 LOS change associated with the 2014–2015 and 2018–2019 unrests. **a** Path 124 LOS change from September 9, 2014 to August 11, 2015 and **b** to May 14, 2019. **c** Topographic relief map lighting from WSW. **d** Path 18 LOS change from November 30, 2017 to July 30, 2015 and **e** to March 21, 2019. **f** Topographic relief map lighting from ESE. Boxes indicate the extracted point of the temporal LOS change shown in Fig. 3. Dashed lines indicate the position of the LOS change cross section in Fig. 4, and thin dashed lines show data extracted regions for LOS change cross section. Black arrows indicate the position of Oana crater

for the temporal baseline of the PALSAR-2 InSAR data unless they were contaminated with strong decorrelation noise. A temporal baseline threshold of 36 days was set for the Sentinel-1 InSAR data.

GAMMA software was used to generate primary InSAR data (Wegmüller and Werner 1997). A power spectrum filter was applied for eliminating uncorrelated noise in each primary InSAR data (Goldstein and Werner 1998) and the minimum cost flow algorithm for phase unwrapping (Costantini 1998). The topographic fringes were corrected by 10 m grid digital elevation model (DEM) provided by the Geospatial Information Authority of Japan. Topography-correlated phase changes, indicating stratified atmospheric delay, were corrected by fitting a linear function to the topographic height. The DEM error, which was proportional to the spatial perpendicular baselines, was simultaneously estimated with displacement rates. A hyperparameter for smoothing temporal variation in the PALSAR-2 data was optimized by using the L-curve criteria (Hansen 1992) (Additional file 1: Fig. S1b, Text S1). We used the hyperparameter values corresponding to the points of maximum curvature in the L-curve plot of the solution norm against the residual norm. To combine the time series of PALSAR-2 and Sentinel-1 LOS changes, we added offsets to the time-series subset of Sentinel-1 LOS change for each year. The adjusted offsets were estimated by minimizing the gap between the PALSAR-2 LOS change and the mean of

Sentinel-1 LOS change acquired for 30 days before and after the acquisition date of each PALSAR-2 data (see Additional file 1: Text S2). A reference point for phase unwrapping was set at approximately 3 km northeast of Oana crater.

## Results

The results of MTI analysis using PALSAR-2 and Sentinel-1 data revealed spatiotemporal variation in ground deformation at Azuma volcano between 2014 and 2020 (Fig. 2, Additional file 1: Figs. S2 and S3). The LOS shortening in 2015 and 2019 was observed at Oana crater and elongated in the northwest–southeast direction (Fig. 2). The LOS shortening in both orbits implied that the uplifts were more dominant than the horizontal displacement components. The time series of PALSAR-2 data at Oana crater showed LOS shortening reaching 10 cm in 2015 and 2019 in Path 124, and 9 cm and 11 cm in 2015 and 2019 in Path 18 with reference to October–November 2017, respectively (Point S and S′ in Fig. 3). These timings of LOS shortening corresponded with the periods of intense seismic activity. Although the first acquisition date of Path 18 PALSAR-2 data was during the period of unrest in 2015, the PALSAR-2 LOS changes for both orbits exhibited similar temporal characteristics throughout the observation period, implying the dominance of the vertical displacement component. The magnitudes of the LOS shortenings associated with the unrest episodes were diminishing in 2016–2017 and late-2019–2020, which corresponds to the quiescent periods (Fig. 3).

Cross section of Path 124 LOS change in the northwest–southeast direction over Oana crater showed that the peak position of LOS shortening in 2019 had shifted approximately 300 m away to the northwest direction from that of 2015 (Fig. 4). Another minor peak of LOS shortening in 2019 was also identified at the peak position of 2015. The northwest–southeast cross section of LOS changes in Path 18 showed that the extent of LOS shortening increased in 2019 towards northwest compared to the extent in 2015 (Fig. 4b). The extension

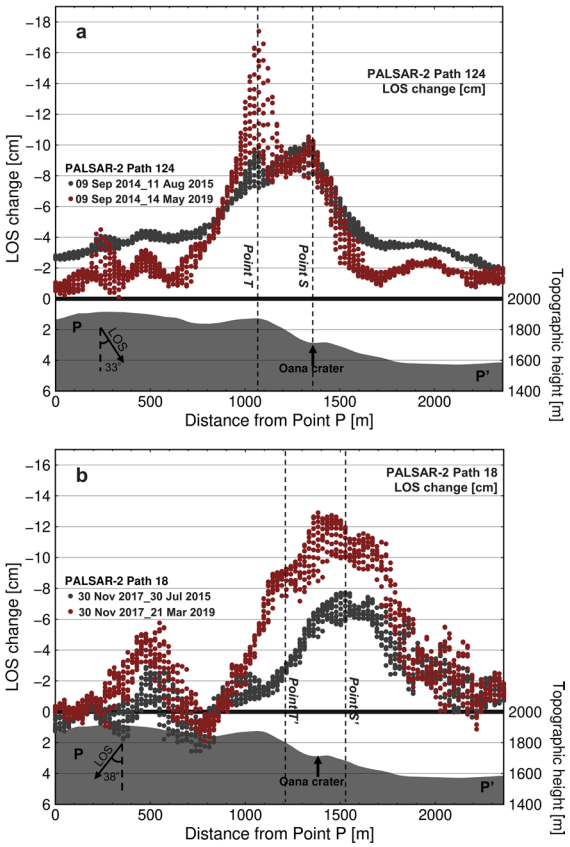


**Fig. 4** Cross section of the PALSAR-2 LOS changes over Oana crater. PALSAR-2 LOS change acquired from **a** Path 124, and **b** Path 18. The original LOS change maps are shown in Fig. 2. The black arrow indicates the position of Oana crater

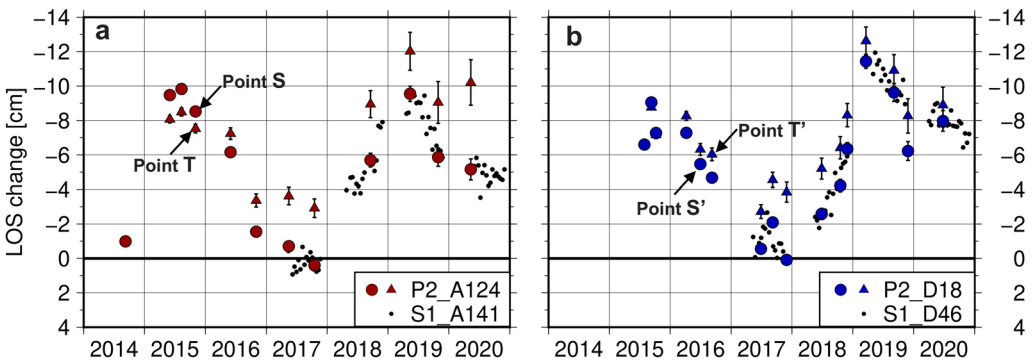


**Fig. 3** Temporal LOS changes on Oana crater. **a**, **b** LOS changes acquired from PALSAR-2 (P2) Path 124 (red circles and triangles) and Sentinel-1 (S1) Path 141 (black dots), and PALSAR-2 Path 18 (blue circles and triangles) and Sentinel-1 Path 46 (black dots). Plots of Sentinel-1 data were extracted on only Point S and S′. The positions of Point S, S′, T, T′ are shown in Fig. 2. Reference dates are October 17, 2017 and November 30, 2017 for P2 A124 and P2 D18, respectively. Incidence angles of PALSAR-2 Path 124 and that of Sentinel-1 Path 141 are 33.2 and 35.3 degrees, respectively

of LOS shortening area implied the spread of pressurized regions associated with the unrest in 2018–2019. A geothermal area was identified approximately 300 m from Oana crater, towards the northwest (JMA 2020; Fig. 1). We extracted another time series of PALSAR-2 LOS changes at this point, 300 m northwest of the deformation peak in 2015 (Fig. 3). During the period between two unrest episodes, we can still identify 4 cm of LOS shortening in Path 124 in the northwest geothermal area on Point T at the time. After the 2018–2019 unrest, the magnitude of LOS shortening at Point S was considerably smaller than that at Point T, and the difference in Path 124 reached approximately 5 cm during mid-2020. Increase in the extent of the deformed area implied the enlargement of the pressurized region associated with the unrest during 2018–2019 which led to geothermal activity at the northwestern part of the geothermal area. The differences in the LOS change in Path 18 between Point S and T were almost constant during the period of 2018–2020. The decomposed quasi-east–west and quasi-vertical displacement maps show about 200–300 m shift of displacement peaks in uplift and that of westward displacement (Fig. 5). The uplift peak in 2019 is located at the extent of the geothermal area which is 300 m northwest of Oana crater.

Another characteristic of deformation was the broad-scale LOS shortening in Path 124 in 2015, distributing from Central Azuma to East Azuma volcano (Fig. 2a, Additional file 1: Fig. S3). The extent of the broad-scale deformation signal was approximately 6 km in the north–south direction and 8 km in the east–west direction. The broader LOS shortening with a maximum amplitude of 2 cm overlapped with the deformation signals at Oana crater (Fig. 5). The broader LOS shortening in 2015 ceased during mid-2017, as did the local deformation on Oana crater. There were no broader deformation signals associated with the unrest in 2018–2019, unlike that of 2015 (Additional file 1: Fig. S3). Two independent InSAR data with different observation periods in 2014–2016 show the broader LOS change at the same extent (Additional file 1: Fig. S4). Therefore, we can regard the identified broader signal as a plausible deformation signal and can eliminate the effect of tropospheric phase delay. For the Path 18 LOS change, we identified no similar broader deformation signals through the observation period.

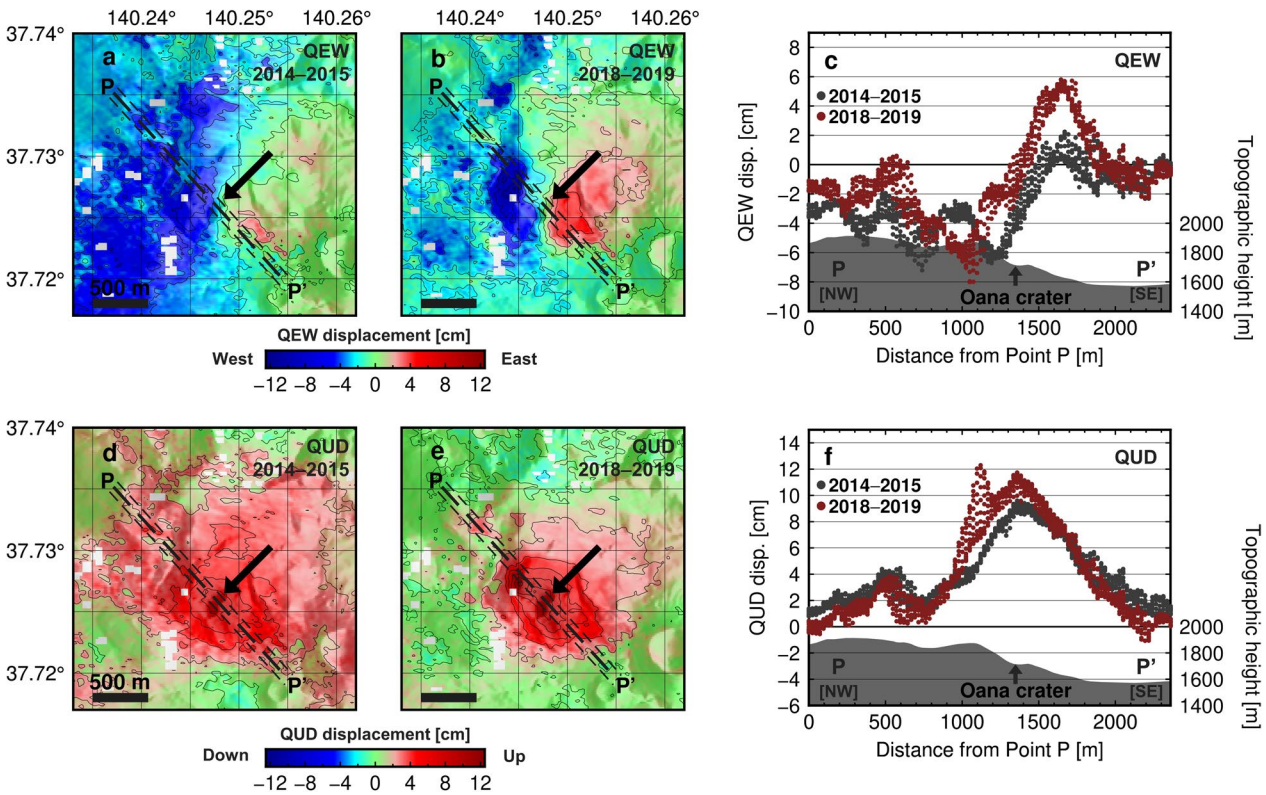


**Fig. 5** Quasi-east–west (QEW) and quasi-vertical (QUD) displacement map and their cross section over Oana crater. **a**–**c** QEW displacement and **d**–**f** quasi-up–down (QUD) displacement component. From the left column, the decomposed displacement associated with the 2014–2015 and 2018–2019 unrests, and the cross sections. Thin dashed lines show data extracted regions for the QEW and QUD cross section

The Sentinel-1 data were used to observe the LOS change with high temporal resolution (approximately every 12 days) from April to November in each year (Additional file 1: Fig. S5). The coherence of Sentinel-1 data on the bare geothermal areas at Oana crater was greater than 0.1 through no snow coverage seasons because of smaller variations in the backscatter characteristics. The Sentinel-1 data we used complements the sparse PALSAR-2 time-series data, although appropriate offsets were required to match the temporal variation in the PALSAR-2 LOS changes (Additional file 1: Table S2). The subsets of the Sentinel-1 LOS changes extracted at Point S in the ascending and at Point S' in the descending orbits were consistent with the temporal variations of the PALSAR-2 LOS change in 2019 in Path 124 and in 2017–2019 in Path 18 (Fig. 3). The temporal variation in the ascending LOS change (Point S) revealed LOS shortening of 4 cm for 2018 and LOS extending of 2 cm for 2020 with approximate variance of 1 cm, although only one PALSAR-2 data was available for these years. We can regard nearly the same observation geometry of PALSAR-2 and Sentinel-1 data, because the incidence angle of PALSAR-2 and Sentinel-1 data at Oana crater were 33.2 and 33.5 degrees, respectively. The extent of the cumulative Sentinel-1 LOS change in 2018 almost coincides with that of the PALSAR-2 LOS shortening in 2018–2019 (Additional file 1: Fig. S5). Based on this, the Sentinel-1 MTI results were limited to the detection of deformation signals only on bare ground during periods with no snow coverage, while successfully revealing high-frequency temporal variations in the LOS change.

#### Modeling of pressure source geometry

Estimating the geometry of the pressure source that induces ground deformation is essential for understanding the structure of subsurface volcanic systems, with regard to the distribution of magma and the existence of pressurized hydrothermal systems. We inferred the geometries of the pressure sources using analytical solutions for ground deformation caused by pressure changes in a point source, a prolate spheroid source, and a rectangular flat source (Mogi 1958; Okada 1985; Yang et al. 1988). These parameters were optimized using the Markov-chain Monte Carlo algorithm with Metropolis–Hasting sampling, which is an approach for stochastic parameter optimization (Hastings 1970). The algorithm reduces computing cost through effective parameter sampling, as opposed to deterministic approaches such as a grid search algorithm. It derives a marginal posterior distribution that elucidates the likelihood of parameter values and their uncertainty. The posterior probability density function $p(\mathbf{m}|\mathbf{d})$ was expressed as

$$p(\mathbf{m}|\mathbf{d}) = \frac{p(\mathbf{d}|\mathbf{m})p(\mathbf{m})}{p(\mathbf{d})}, \quad (1)$$

where $p(\mathbf{d}|\mathbf{m})$ is the likelihood function of $\mathbf{d}$ given that model $\mathbf{m}$, $p(\mathbf{m})$ is a priori probability density function, and $p(\mathbf{d})$ is a normalized constant. The observed data were subsampled based on the quad-tree algorithm to reduce computing costs and the remaining spatial features of the deformation fields (Jónsson et al. 2002). The number of data and variances are as presented in Additional file 1: Table S3. A Poisson's ratio of 0.25 was assigned when computing surface deformation. In our modeling, we assigned height offsets to each subsampled data point for the first-order approximation of the topography effect when computing surface displacements using analytical solutions (Williams and Wadge 1998). First, we fitted the broader deformation signal in Path 124 PALSAR-2 LOS change in 2015 to infer the pressure source geometry. Based on the best-fit geometry of the pressure source for the broader deformation in 2015, we subtracted the broader deformation signal from the original Path 124 LOS change to isolate the local deformation signals at Oana crater (Additional file 1: Fig. S6). Next, we inferred geometries of the pressure sources using a set of LOS changes showing the local deformation at Oana crater for PALSAR-2 Path 18 and 124. The prior ranges for solution spaces in each model are shown in Additional file 1: Tables S4–S6. The corner plot of parameters for each model are shown in Additional file 1: Figs. S7–S15. We regard a parameter combination of each model that minimizes AIC values as the best-fit model in this study.

For the broader deformation in 2015, a horizontal rectangular source (sill) was the best-fit model in terms of compared to those of a spheroid or a point source (Additional file 1: Table S7, Fig. S16). The best-fit sill position was inferred at 360 m b.s.l.in the east to approximately 1500 m b.s.l. in the west (Fig. 6). The extent of the sill almost covered the region with the broad deformation signals (Additional file 1: Fig. S16). The best-fit sill was not reproduced the local deformation at Oana crater, and it became one of the input data for modeling geometry of the shallowest pressure source in the next step. Although the modeled geometry was constrained by only a PALSAR-2 Path 124 LOS change, the flat source was a plausible geometry for the broader deformation in 2015. The best-fit synthetic deformation was employed to correct the broader deformation signal in the original Path 124 LOS change in 2015 for the next step (Additional file 1: Fig. S6).

For the geometry of the local deformation at Oana crater, a prolate spheroid source was the best-fit model in terms of AIC value for the 2015 and 2019 data (Additional file 1: Figs. S17, S18, Table S7). The prolate spheroid sources were located beneath Oana crater and elongated

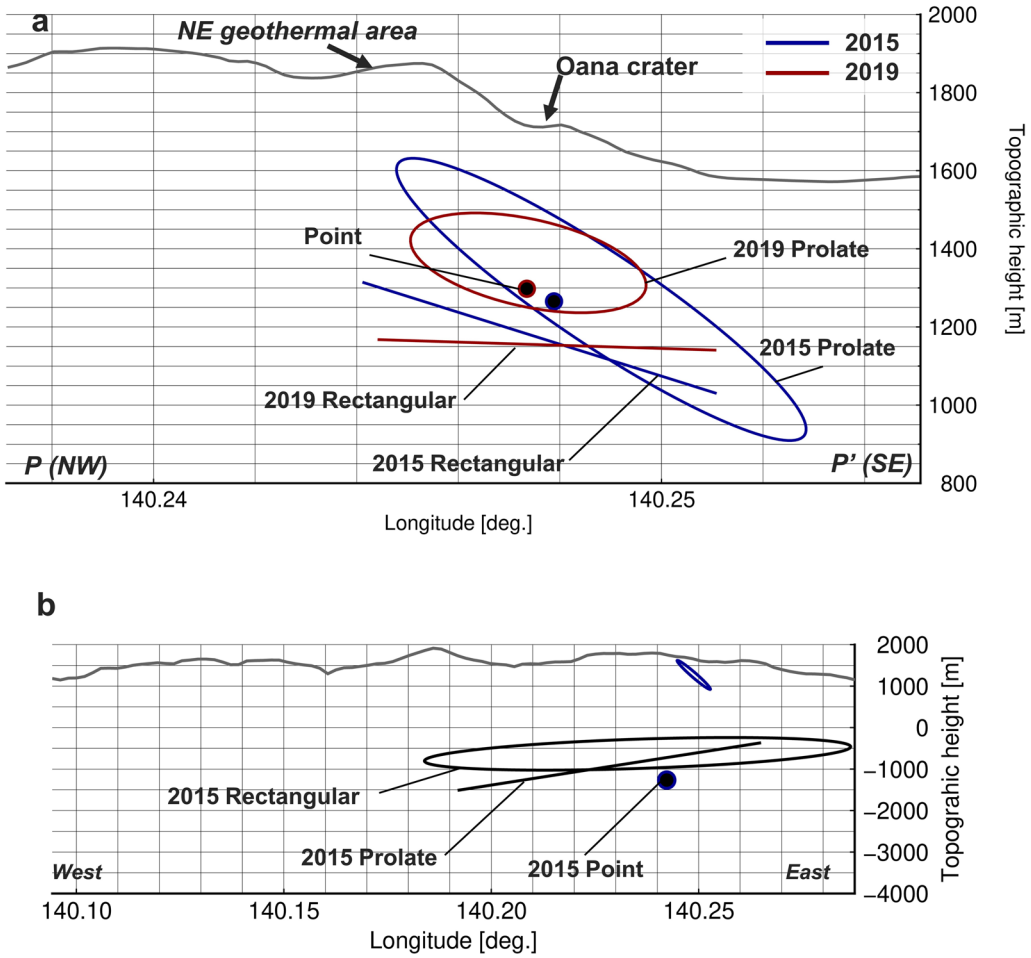


**Fig. 6** Schematic of modeled geometry of the pressure source for the observation data. **a** Longitudinal projection of pressure source geometry for the local deformation around Oana crater and **b** for the broader deformation in 2015. Blue and red symbols indicate the outline of the pressure source geometry for the data in 2015 and 2019, respectively. Gray lines show a topographic height cross section at Profile P–P′ in **a** and a cross section in longitude direction at N37.724° in **b**

in a northwest–southeast direction. The best-fit geometries of the prolate spheroid dips towards the southeast, and these angles were similar to the topographic slope around Oana crater (Fig. 6a; Additional file 1: Fig. S19). The similar characteristics was also suggested in the best-fit geometry of sill. The inferred pressure source for the local deformation on Oana crater were inferred to be located 1270–1360 m a.s.l.. The strike angle of the major axis of the prolate spheroid (20–60 degrees anti-clockwise from the north) was similar azimuth angle with the alignment of the pyroclastic cone of East Azuma volcano in the northwest–southeast direction (Figs. 1 and 7). The similarity between the strike angle of the spheroid major axis and that of the alignment of the pyroclastic cones at East Azuma volcano implies the shallow stress regime, rather than the far-field east–west compressional stress regime which is induced by plate motion (Terakawa and Matsu'ura 2010; Uchide et al. 2022). Pressure sources with a prolate spheroid geometry have been previously proposed as inducing deformation in geothermal areas (Fialko and Simons 2000; Juncu et al. 2017).

## Discussion

### Implications for the shallow hydrothermal system of Azuma volcano

For the prolate spheroid as a deformation source, rigidity is required to assign for evaluating the pressure changes. When assigning the rigidity of 1.0 GPa which is a plausible value for shallower depths in the geothermal area (Lynne et al. 2013), the overpressure of the derived prolate spheroid becomes 2.2–4.3 MPa (Additional file 1: Table S5). The continuous emission of volcanic gas and steam from Oana crater since 2000 implies a continuous supply of heat or hydrothermal fluid from the depths. This phenomenon would cause hydrothermal alteration of the crust due to the continuous contact of

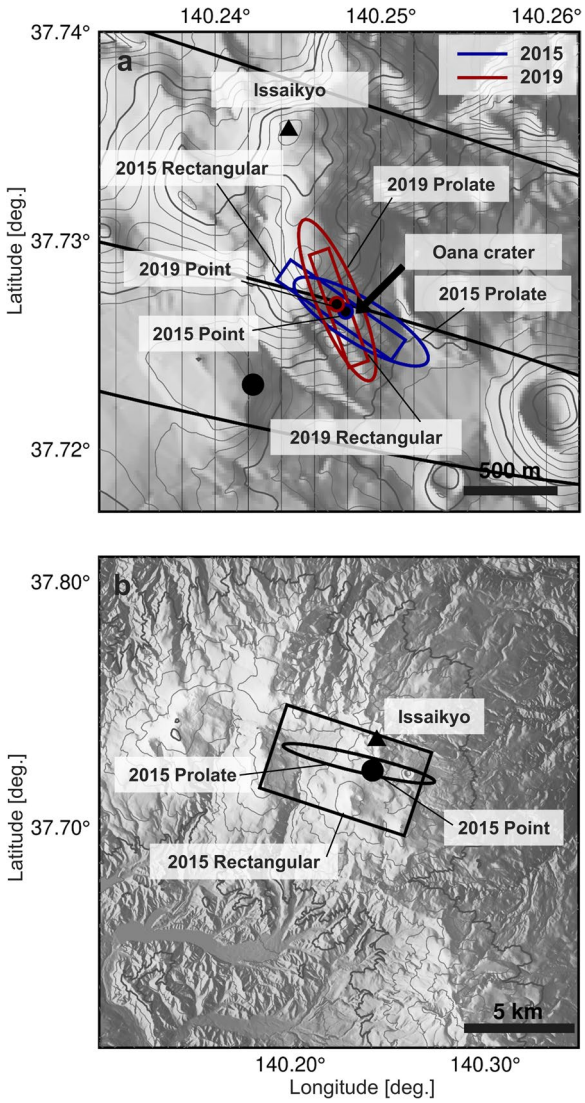


**Fig. 7** Two-dimensional map of the pressure source geometry for the observation data. The details are the same for Fig. 6

the high-temperature hydrothermal fluid with volcanic rocks. This hydrothermal alteration has the potential to induce variation in the permeability and porosity of volcanic rocks which controls the elastic moduli (Browne 1978; Wyering et al. 2014; Heap et al. 2017, 2020). Evolution of fractures or the variation of the chemical properties of minerals, such as dissolution, precipitation, or sulphates, causes an increase in porosity, while filling materials into microcracks decreases porosity. Wyering et al. (2014) proposed that altered rock samples with low or moderate temperatures and at shallower depths had smaller densities and larger porosity, although these were also impacted by other factors, such as primary rock property. The elastic moduli become smaller due to the hydrothermal alteration at shallower depths, which requires smaller pressure changes; however, more petrological evidence is necessary for supporting this assumption.

Volcano-tectonic and low-frequency earthquakes were reported at shallower depths ranging 1500 m a.s.l. to 500 m b.s.l. around Oana crater due to the unrest episodes in 2014–2015 and 2018–2019 (JMA 2020). Volcano-tectonic earthquakes imply the occurrence of brittle failures of rock, and low-frequency earthquakes on active volcanoes are caused by the excitation of a fluid-crack system, implying the migration of magmatic fluid or magma (Ukawa and Ohtake 1987; Kaneshima et al. 1996; Kumagai and Chouet 1999). The characteristics of volcano-tectonic earthquakes suggest magmatic fluid migration, inducing overpressure that causes brittle failures within or around the volcanic system of Azuma volcano (Wicks et al. 1998; Hurwitz et al. 2007). In the case of the 2018–2019 unrest, an increase in the composition ratio of $SO_2/H_2S$ within a fumarole from Oana crater implies the supply of high-temperature volcanic gas from greater depths (JMA 2020). A geological survey proposed that eruptions or unrests

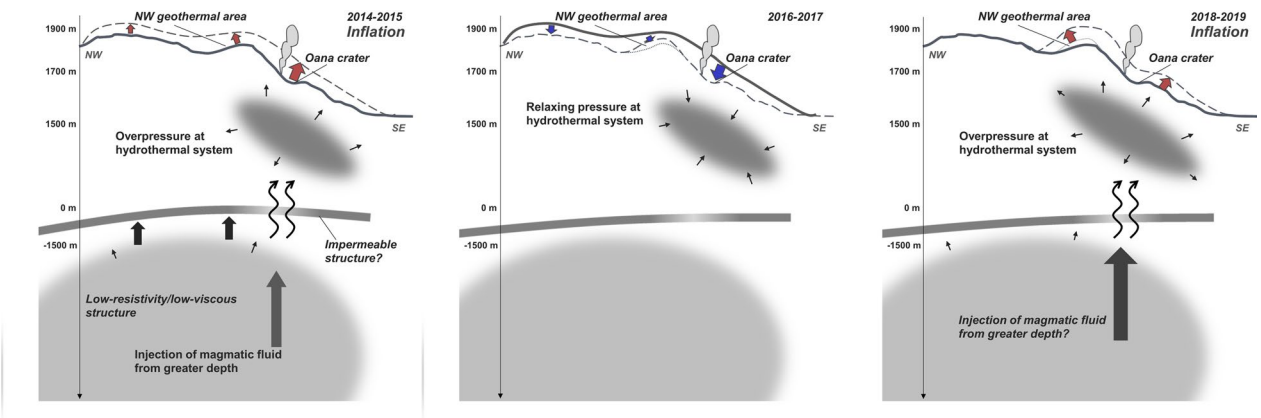


**Fig. 8** Schematic image of the pressure sources beneath Azuma volcano. Note that the diagram is for explanation purpose only and is not to scale

since the 1711 eruption were related to overpressure at shallow hydrothermal system (Yamamoto 2005). Thus, these unrests are also related to the overpressure at the hydrothermal system.

For the local deformation at Oana crater, the correlation between the topographic feature around Oana crater and the geometry of best-fit pressure sources suggests the existence of a possible pre-existing impermeable structure with a layered topography-correlated structure, rather than a horizontal layered structure (Fig. 8; Additional file 1: Fig. S19). The standard deviation of the plunge angle for the best-fit prolate sphere was about 15 degrees (Additional file 1: Table S5, Figs. S11 and S12). The narrower marginal posterior distribution of the plunge angle, compared to that of the pressure change or the aspect ratio of the major and minor axes, implies a better fit of the plunge angle (Additional file 1: Figs. S11 and S12). Variation in plunge angles for the prolate spheroid result in variations in both the magnitude and spatial characteristics of deformation, and these differences are enough to distinguish them from the best-fit synthetic deformations (Additional file 1: Fig. S20).

Another potential factor contributing to the overpressure of the hydrothermal system is the increasing temperature due to heat transfer from the greater depths. We examined the pressure change that caused such temperature changes in the hydrothermal system. The overpressure associated with volumetric expansion can be caused by an increase in temperature of a hydrothermal system. Based on the state equation, the pressure change $\mathrm{d}p$ is expressed as a function of the volume $V$ and temperature $T$ as follows:

$$\mathrm{d}p = \left(\frac{\partial p}{\partial V}\right)_T \mathrm{d}V + \left(\frac{\partial p}{\partial T}\right)_V \mathrm{d}T. \tag{2}$$

Based on the definition of the bulk modulus of water $k_\mathrm{f}$ and the coefficient of thermal expansion of fluid $\alpha_\mathrm{f}$, Eq. (2) becomes:

$$\Delta p = -k_\mathrm{f}\frac{\Delta V}{V} + \alpha_\mathrm{f} k_\mathrm{f} \Delta T. \tag{3}$$

The ratio of the volume change of the spheroid $\Delta V/V$ is given by a function of the pressure change $\Delta p$ and the rigidity of the medium $\mu$, where $\Delta V/V = (3/4\mu)\Delta p$, such that (Segall 2010):

$$\Delta T = \left(\frac{1}{k_\mathrm{f}} + \frac{3}{4\mu}\right)\frac{\Delta p}{\alpha_\mathrm{f}}. \tag{4}$$

For the shallower hydrothermal system, the range of the best-fit pressure increase was between 2.2 and 4.3 MPa for a prolate spheroid beneath Oana crater under the assumption of rigidity $\mu$ of 1.0 GPa (Lynne et al. 2013; Lesage et al. 2018). The bulk modulus of water and the coefficient of fluid expansion at 60 °C were assigned to $2.0\times10^9$ Pa and $0.3\times10^{-3}$ K$^{-1}$, respectively (see Additional file 1: Text S3). By assigning the values for these parameters, we can estimate that the inferred pressure change was altered by a temperature change of 9.3–17.8 K. This pressure change corresponded to a 0.17–0.32% increase in volume, if the volume change was caused by fluid expansion that occurred due to an increase in temperature. A geothermal survey reported that the surface temperature of the geothermal area around Oana crater increased by approximately 20 K compared to the temperature before the unrest in 2018–2019 (JMA 2020). The inferred increase in the temperature was sufficient to induce volumetric expansion of water within the shallow hydrothermal system. However, we consider that the thermal expansion of the water within the shallow hydrothermal system is not the unique mechanism to induce the detected deformation because the number of volcanic earthquakes and of low-frequency earthquakes increased during the unrest.

In contrast, deflation at volcanoes related to hydrothermal activity is interpreted as a mechanical response to decrease in pore pressure that is caused by the diffusion of magmatic volatile or heat (Fialko and Simons 2000; Todesco et al. 2004; Peltier et al. 2009), poroelastic contraction (Barbour et al. 2016). In this case, the volcanic volatiles that were supplied from deeper depths during the unrest were mainly diffused laterally or downward through porous rock, rather than from the active craters or the geothermal areas (Denlinger 1997; Nakaboh et al. 2003). This is because the maximum fumarole height from Oana crater remained stable through the observation period. Similar cyclic pattern of uplift and subsidence at volcanoes was also proposed to be induced by change in pore pressure within shallow hydrothermal system in response to variation of heat or gas flux (Peltier et al. 2009). Drain-back or thermal contraction of magma also induces subsidence as a post-process of magma ascent or emplacement (Watanabe et al. 1998; Fujiwara et al. 2017), however no evidence of magma ascent has been reported during the unrests in 2014–2015 and 2018–2019. Therefore, the deflations during the post-unrest periods can be interpreted as a relaxation of pressure within the hydrothermal system, likely resulting from the diffusion of volcanic volatile.

Detailed structures of the two pressure sources were inferred from satellite SAR data, modeled geometry, and the above discussion (Fig. 8). It is challenging to identify the certain physical mechanism inducing the ground deformation of Azuma volcano, since several processes can be acceptable explanations for the ground

deformation. Although satellite SAR data can be used to reveal ground deformation with high spatial resolution, other observation data are required to support the interpretation of the SAR data processing results.

#### Deeper pressure source inducing the broad deformation

Although the broad deformation was detected in PALSAR-2 LOS change in Path 124 in 2015, we could not detect such similar broad deformation signals associated with the 2018–2019 unrest (Additional file 1: Fig. S3). In contrast, continuous GNSS data showed increases in the short (~1 km, over Oana crater) and long (>10 km, over the eastern side of Azuma volcano) baselines, which crossed the cluster position of the deep low-frequency earthquake at depths of 20–40 km b.s.l. (JMA 2020). The magnitude of the GNSS baseline change was similar in 2014–2015 and 2018–2019. The increases of both short GNSS baseline crossing Oana crater and long GNSS baselines crossing Azuma volcano were almost simultaneously initiated in relation to the unrest episodes of 2014–2015 and 2018–2019. This suggests instantaneous propagation of pressure changes from greater depths.

A bandpass filter is sometimes applied to eliminate spatially correlated phase changes, such as tropospheric phase screens or residuals of phase change correction that are proportional to the baselines when applying the SAR time-series analysis. Spatial filtering has the potential to eliminate the broad deformation signals because of the similar spatial correlation distance of a few kilometers and the tropospheric phase screen. In this case, we ruled out this possibility because we did not apply a spatial filter for the SAR time-series data. Although we corrected topography-correlation signals in each InSAR dataset to eliminate the effect of stratified water vapor distribution, similar broad deformations should have been detected if the spatial characteristics were similar to those detected in 2015. Combinations of geodetic observations, such as GNSS and tiltmeter data, would be effective in improving the robustness of monitoring broad ground deformations.

The extent of broader LOS shortening in Path 124 in 2015 almost overlapped with that of the LOS extending (maximum of 9 cm) in 2011, that was caused by the 2011 Tohoku–Oki earthquake (Additional file 1: Fig. S21). The LOS extending for 2011 was derived by subtracting the original ALOS/PALSAR InSAR data from the co-seismic displacement of the Tohoku–Oki earthquake approximated by a quadratic surface (Additional file 1: Fig. S21). The best-fit model geometry for the broad deformation in 2015 was a flat-source located at approximately 360–1500 m b.s.l. Volcanic earthquakes were absent across most of the extent of the flat-source, except beneath Oana crater (JMA 2020). A previous magnetotelluric survey revealed a convex-shaped low-resistivity structure in the east–west direction and north–south direction at depths of 3–10 km b.s.l. and 3–15 km b.s.l., respectively, composed of a dacitic melt–rock–hydrothermal fluid complex (Ichiki et al. 2021). The horizontal extent of the shallowest region of the low resistivity structure was almost consistent with the extent of the broad deformation in 2015, although the modeled flat-source depth was approximately 1.5 km away from the top position of the low resistivity structure or approximately 240–900 m away from the top of the low viscous body (Takada and Fukushima 2013; Ichiki et al. 2021). Based on the results of our modeling and findings from previous surveys, the modeled flat-source can be interpreted as barriers to fluid and volatile migration within the dacitic melt–rock–hydrothermal fluid complex, serving as a part of impermeable structure, rather than as a magmatic body (Christenson et al. 2010). Impermeable structures distributed above hydrothermal systems accumulate pressure within the hydrothermal system (Kaneshima et al. 1996; Stix and de Moor 2018). Assuming that the impermeable layer was located above the dacitic melt–rock–hydrothermal fluid complex, a portion of the impermeable layer beneath Oana crater was of low density or broken, and allowed the passage of ascending magmatic fluids from greater depths (Fig. 8).

## Conclusion

We investigated the spatiotemporal variation in ground deformations at Azuma volcano (Japan) during 2014–2020 based on the results of MTI analysis and the geometries of pressure sources that caused ground deformations associated with the 2014–2015 and 2018–2019 volcanic unrest episodes.

The PALSAR-2 MTI results revealed repeated inflations with peaks in 2015 and 2019, which corresponded with periods that showed an increase in volcanic earthquakes beneath Oana crater. Sentinel-1 MTI results showed deformation signals with almost 12 days of temporal resolution only in the exposed geothermal regions (Oana crater) during periods with no snow coverage. These results could enhance the temporal characteristics of the sparse PALSAR-2 LOS changes by adding suitable offsets.

Our model proposed the following best-fit geometries of pressure source for the detected ground deformation at Azuma volcano: a centroid of the prolate spheroid located at a depth of 1270–1360 m a.s.l. for the local deformation of Oana crater and a horizontal flat source at approximately 360–1500 m b.s.l. for the broader deformation observed in 2015. Not only the supply of the magmatic fluids from deeper depths but also the volumetric expansion due to an increase in

temperature can also be a potential explanation for the overpressure inducing the local inflation centering at Oana crater. The flat-source for the broader deformation can be interpreted as an upper portion of barriers of fluids or volatile migration within the dacitic melt–rock–hydrothermal fluid complex as suggested by a previous magnetotelluric survey.

The continuous fumarole from Oana crater and unrest episodes at Azuma volcano imply a potential for continuous inflow of volcanic gas or fluids from deeper depths. Frequent observations from next-generation L-band SAR satellites in the future could help improve the temporal resolution of ground deformation monitoring, even in cases where the volcanoes are covered with dense vegetation. To elucidate the pressure conditions in shallower hydrothermal systems, it is necessary to enhance the time-dependent numerical modeling by incorporating the circulation of magmatic–hydrothermal fluid and considering heat transfer within a porous medium.

#### Abbreviations

| | |
|---|---|
| SAR | Synthetic aperture radar |
| InSAR | Interferometric synthetic aperture radar |
| JMA | Japan Meteorological Agency |
| GNSS | Global Navigation Satellite System |
| ALOS | Advanced land observing satellite |
| PALSAR | Phased-array L-band synthetic aperture radar |
| LOS | Line-of-sight |
| MTI | Multi-temporal InSAR |
| DEM | Digital elevation model |
| AIC | Akaike's Information Criterion |
| QEW | Quasi-east–west |
| QUD | Quasi-up–down |

## Supplementary Information

The online version contains supplementary material available at https://doi.org/10.1186/s40623-024-01988-8.

**Additional file 1.** "Supplementary figures and tables."

#### Acknowledgements

We are grateful to the Editor-in-Chief and the Editor for handling our manuscript, and to two anonymous reviewers for providing constructive comments. PALSAR level 1.0 and PALSAR-2 level 1.1 data in this study were shared among a Japan InSAR consortium PIXEL and provided from JAXA under a cooperative research contract with the PIXEL (PI No. ER2A2N187). The ownership of PALSAR data belongs to the Ministry of Economy, Trade, and Industry (METI) and JAXA, and that of PALSAR-2 data belongs to JAXA. This study is supported by ERI JURP 2018-B-02 and 2021-B-03.

#### Author contributions

YH contributed to conceptualization, data processing, modeling, drafting the manuscript. TO contributed to conceptualization, project administration, supervision and revising the manuscript. All authors read and approved the final manuscript.

#### Funding

This study was conducted under the framework of Subtheme 2-1, Project B of "Integrated program for next generation volcano research and human resource development" led by the Ministry of Education, Culture, Sport, Science and Technology, Japan (MEXT).

#### Availability of data and materials

ALOS/PALSAR level 1.0 and ALOS2/PALSAR2 level 1.1 data can be searched and purchased from either RESTEC (https://www.restec.or.jp/en/) or PASCO (http://en.alos-pasco.com). Sentinel-1 data are freely available from Sentinel data hub website (https://scihub.copernicus.eu/). GAMMA software is developed by Gamma Remote Sensing (https://www.gamma-rs.ch).

## Declarations

#### Competing interests

The authors declare that the research was conducted without any commercial or financial relationships that could potentially lead to conflicts of interest.

#### Author details

[1]Earthquake Research Institute, The University of Tokyo, Tokyo, Japan. [2]National Research Institute for Earth Science and Disaster Resilience, Tsukuba, Japan.

Received: 23 April 2023 Accepted: 24 February 2024
Published online: 13 March 2024

#### References

Amelung F, Jonsson S, Zebker H, Segall P (2000) Widespread uplift and "trapdoor" faulting on Galapagos volcanoes observed with radar interferometry. Nature 407(6807):993–996. https://doi.org/10.1038/35039604

Ban M, Takebe Y, Adachi T, Matsui R, Nishi Y (2016) Eruption histories of Zao and Azuma volcanoes and their magma feeding systems for recent activities. Bull Earthq Res Inst Univ Tokyo 91(3):25–39

Barbour AJ, Evans EL, Hickman SH, Eneva M (2016) Subsidence rates at the southern Salton Sea consistent with reservoir depletion. J Geophys Res Solid Earth 121(7):5308–5327. https://doi.org/10.1002/2016JB012903

Berardino P, Fornaro G, Lanari R, Sansosti E (2002) A new algorithm for surface deformation monitoring based on small baseline differential SAR interferograms. IEEE Trans Geosci Remote Sens 40(11):2375–2383. https://doi.org/10.1109/TGRS.2002.803792

Browne PRL (1978) Hydrothermal alteration in active geothermal fields. Annu Rev Earth Planet Sci 6(1):229–248. https://doi.org/10.1146/annurev.ea.06.050178.001305

Christenson BW, Reyes AG, Young R, Moebis A, Sherburn S, Cole-Baker J, Britten K (2010) Cyclic processes and factors leading to phreatic eruption events: insights from the 25 September 2007 eruption through Ruapehu Crater Lake, New Zealand. J Volcanol Geotherm Res 191(1–2):15–32. https://doi.org/10.1016/j.jvolgeores.2010.01.008

Costantini M (1998) A novel phase unwrapping method based on network programming. IEEE Trans Geosci Remote Sens 36(3):813–821. https://doi.org/10.1109/36.673674

Denlinger RP (1997) A dynamic balance between magma supply and eruption rate at Kilauea volcano. Hawaii J Geophys Res Solid Earth 102(B8):18091–18100. https://doi.org/10.1029/97jb01071

Doke R, Mannen K, Itadera K (2021) Observing posteruptive deflation of hydrothermal system using InSAR time series analysis: an application of ALOS-2/PALSAR-2 data on the 2015 phreatic eruption of Hakone volcano, Japan. Geophys Res Lett 48(19):e2021GL094880. https://doi.org/10.1029/2021GL094880

Feigl KL, Gasperi J, Sigmundsson F, Rigo A (2000) Crustal deformation near Hengill volcano, Iceland 1993–1998: coupling between magmatic activity and faulting inferred from elastic modeling of satellite radar interferograms. J Geophys Res Solid Earth 105(B11):25655–25670. https://doi.org/10.1029/2000JB900209

Fialko Y, Simons M (2000) Deformation and seismicity in the Coso geothermal area, Inyo County, California: observations and modeling using satellite radar interferometry. J Geophys Res Solid Earth 105(B9):21781–21793. https://doi.org/10.1029/2000JB900169

Fujiwara S, Murakami M, Nishimura T, Tobita M, Yarai H, Kobayashi T (2017) Volcanic deformation of Atosanupuri volcanic complex in the Kussharo caldera, Japan, from 1993 to 2016 revealed by JERS-1, ALOS, and ALOS-2

radar interferometry 5. Volcanology. Earth Planets Space 69(1):1–14. https://doi.org/10.1186/s40623-017-0662-y
Goldstein RM, Werner CL (1998) Radar interferogram filtering for geophysical applications. Geophys Res Lett 25(21):4035. https://doi.org/10.1029/1998GL900033
Hamling IJ, Williams CA, Hreinsdõttir S (2016) Depressurization of a hydrothermal system following the August and November 2012 Te Maari eruptions of Tongariro, New Zealand. Geophys Res Lett 43(1):168–175. https://doi.org/10.1002/2015GL067264
Hansen PC (1992) Analysis of discrete ill-posed problems by means of the L-curve. SIAM Rev 34(4):561–580. https://doi.org/10.1137/1034115
Hastings WK (1970) Monte carlo sampling methods using Markov chains and their applications. Biometrika 57(1):97–109. https://doi.org/10.1093/biomet/57.1.97
Heap MJ, Kennedy BM, Farquharson JI, Ashworth J, Mayer K, Letham-Brake M, Reuschlé T, Gilg HA, Scheu B, Lavallée Y, Siratovich P, Cole J, Jolly AD, Baud P, Dingwell DB (2017) A multidisciplinary approach to quantify the permeability of the Whakaari/White Island volcanic hydrothermal system (Taupo Volcanic Zone, New Zealand). J Volcanol Geotherm Res 332:88–108. https://doi.org/10.1016/j.jvolgeores.2016.12.004
Heap MJ, Villeneuve M, Albino F, Farquharson JI, Brothelande E, Amelung F, Got JL, Baud P (2020) Towards more realistic values of elastic moduli for volcano modelling. J Volcanol Geotherm Res 390:106684. https://doi.org/10.1016/j.jvolgeores.2019.106684
Hurwitz S, Christiansen LB, Hsieh PA (2007) Hydrothermal fluid flow and deformation in large calderas: inferences from numerical simulations. J Geophys Res Solid Earth 112(2):1–16. https://doi.org/10.1029/2006JB004689
Ichiki M, Kaida T, Nakayama T, Miura S, Yamamoto M, Morita Y, Uyeshima M (2021) Magma reservoir beneath Azumayama volcano, NE Japan, as inferred from a three-dimensional electrical resistivity model explored by means of magnetotelluric method. Earth Planets Space 73(1):1–30. https://doi.org/10.1186/s40623-021-01451-y
Japan Meteorological Agency (2020) Summary of the volcanic activity on Azuma volcano, issued in the 147th Coordinating Committee for the Prediction of Volcanic Eruption (CCPVE). https://www.data.jma.go.jp/svd/vois/data/tokyo/STOCK/kaisetsu/CCPVE/shiryo/147/147_3-2.pdf. Accessed 20 Dec 2021 (**in Japanese**)
Jolly AD, Sherburn S, Jousset P, Kilgour G (2010) Eruption source processes derived from seismic and acoustic observations of the 25 September 2007 Ruapehu eruption-North Island, New Zealand. J Volcanol Geotherm Res 191(1–2):33–45. https://doi.org/10.1016/j.jvolgeores.2010.01.009
Jónsson S, Zebker H, Segall P, Amelung F (2002) Fault slip distribution of the 1999 Mw7.1 Hector Mine, California, earthquake, estimated from satellite radar and GPS measurements. Bull Seismol Soc Am 92:1377–1389
Juncu D, Árnadóttir T, Hooper A, Gunnarsson G (2017) Anthropogenic and natural ground deformation in the Hengill geothermal area, Iceland. J Geophys Res Solid Earth 122(1):692–709. https://doi.org/10.1002/2016JB013626
Kaneshima S, Kawakatsu H, Matsubayashi H, Sudo Y, Tsutsui T, Ohminato T, Ito H, Uhira K, Yamasato H, Oikawa J, Takeo M, Iidaka T (1996) Mechanism of phreatic eruptions at Aso volcano inferred from near-field broadband seismic observations. Science 273(5275):642–645. https://doi.org/10.1126/science.273.5275.642
Kato A, Terakawa T, Yamanaka Y, Maeda Y, Horikawa S, Matsuhiro K, Okuda T (2015) Preparatory and precursory processes leading up to the 2014 phreatic eruption of Mount Ontake, Japan. Earth Planets Space 67(1):1–11. https://doi.org/10.1186/s40623-015-0288-x
Kawanabe Y, Ueki S (2013) Azumayama. In: Japan Meteorological Agency, The Volcanological Society of Japan (eds) National catalogue of the active volcanoes in Japan, 4th edn. Japan Meteorological Agency, Tokyo. https://www.data.jma.go.jp/svd/vois/data/tokyo/STOCK/souran_eng/volcanoes/034_azumayama.pdf
Kobayashi T, Morishita Y, Munekane H (2018) First detection of precursory ground inflation of a small phreatic eruption by InSAR. Earth Planet Sci Lett 491:244–254. https://doi.org/10.1016/j.epsl.2018.03.041
Kumagai H, Chouet BA (1999) The complex frequencies of long-period seismic events as probes of fluid composition beneath volcanoes. Geophys J Int 138(2):7–12. https://doi.org/10.1046/j.1365-246X.1999.00911.x
Lesage P, Heap MJ, Kushnir A (2018) A generic model for the shallow velocity structure of volcanoes. J Volcanol Geotherm Res 356:114–126. https://doi.org/10.1016/j.jvolgeores.2018.03.003
Lynne BY, Pender M, Glynn-Morris T, Sepulveda F (2013) Combining scanning electron microscopy and compressibility measurement to understand subsurface processes leading to subsidence at Tauhara Geothermal Field, New Zealand. Eng Geol 166:26–38. https://doi.org/10.1016/j.enggeo.2013.08.008
Maeda Y, Kumagai H, Lacson R, Figueroa MS, Yamashina T, Ohkura T, Baloloy AV (2015) A phreatic explosion model inferred from a very long period seismic event at Mayon Volcano, Philippines. J Geophys Res Solid Earth 120(1):226–242. https://doi.org/10.1002/2014JB011440
Mogi K (1958) Relations between the eruptions of various volcanoes and the deformations of the ground surfaces around them. Bull Earthq Res Inst 36(2):99–134
Nakaboh M, Ono H, Sako M, Sudo Y, Hashimoto T, Hurst AW (2003) Continuing deflation by fumaroles at Kuju volcano, Japan. Geophys Res Lett 30(7):1–4. https://doi.org/10.1029/2002GL016047
Narita S, Ozawa T, Aoki Y, Shimada M, Furuya M, Takada Y, Murakami M (2020) Precursory ground deformation of the 2018 phreatic eruption on Iwo-Yama volcano, revealed by four-dimensional joint analysis of airborne and spaceborne InSAR. Earth Planets Space 72(1):1–16. https://doi.org/10.1186/s40623-020-01280-5
Okada Y (1985) Surface deformation due to shear and tensile faults in a half-space. Bull Seismol Soc Am 75(4):1135–1154
Okada T, Yoshida K, Ueki S, Nakajima J, Uchida N, Matsuzawa T, Umino N, Hasegawa A (2011) Shallow inland earthquakes in NE Japan possibly triggered by the 2011 off the Pacific coast of Tohoku Earthquake. Earth Planets Space 63(7):749–754. https://doi.org/10.5047/eps.2011.06.027
Ozawa T, Fujita E (2013) Local deformations around volcanoes associated with the 2011 off the Pacific coast of Tohoku earthquake. J Geophys Res Solid Earth 118(1):390–405. https://doi.org/10.1029/2011JB009129
Peltier A, Scott B, Hurst T (2009) Ground deformation patterns at White Island volcano (New Zealand) between 1967 and 2008 deduced from levelling data. J Volcanol Geotherm Res 181(3–4):207–218. https://doi.org/10.1016/j.jvolgeores.2009.01.020
Pritchard ME, Jay JA, Aron F, Henderson ST, Lara LE (2013) Subsidence at southern Andes volcanoes induced by the 2010 Maule, Chile earthquake. Nat Geosci 6(8):632–636. https://doi.org/10.1038/ngeo1855
Schmidt DA, Bürgmann R (2003) Time-dependent land uplift and subsidence in the Santa Clara valley, California, from a large interferometric synthetic aperture radar data set. J Geophys Res Solid Earth 108(B9):1–13. https://doi.org/10.1029/2002JB002267
Segall P (2010) Earthquake and volcano deformation. Princeton University Press, Princeton, p 432
Stix J, de Moor JM (2018) Understanding and forecasting phreatic eruptions driven by magmatic degassing. Earth Planets Space 70(1):1–19. https://doi.org/10.1186/s40623-018-0855-z
Takada Y, Fukushima Y (2013) Volcanic subsidence triggered by the 2011 Tohoku earthquake in Japan. Nat Geosci 6(8):637–641. https://doi.org/10.1038/ngeo1857
Terakawa T, Matsu'ura M (2010) The 3-D tectonic stress fields in and around Japan inverted from centroid moment tensor data of seismic events. Tectonics. https://doi.org/10.1029/2009TC002626
Todesco M, Rutqvist J, Chiodini G, Pruess K, Oldenburg CM (2004) Modeling of recent volcanic episodes at Phlegrean Fields (Italy): geochemical variations and ground deformation. Geothermics 33(4):531–547. https://doi.org/10.1016/j.geothermics.2003.08.014
Uchide T, Shiina T, Imanishi K (2022) Stress map of Japan: detailed nationwide crustal stress field inferred from focal mechanism solutions of numerous microearthquakes. J Geophys Res Solid Earth 127(6):e2022JB024036. https://doi.org/10.1029/2022JB024036
Ukawa M, Ohtake M (1987) A monochromatic earthquake suggesting deep-seated magmatic activity beneath the Izu-Ooshima volcano, Japan. J Geophys Res 92(B12):12649. https://doi.org/10.1029/jb092ib12p12649
Watanabe H, Okubo S, Sakashita S, Maekawa T (1998) Drain-back process of basaltic magma in the summit conduit detected by microgravity observation at Izu-Oshima volcano, Japan. Geophys Res Lett 25(15):2865–2868. https://doi.org/10.1029/98GL02216

Wegmüller U, Werner CL (1997) Gamma SAR processor and interferometry software. In: Proc. of the 3rd ERS symposium, European Space Agency Special Publication, ESA SP-414, pp 1687–1692

Wicks C, Thatcher W, Dzurisin D (1998) Migration of fluids beneath yellowstone caldera inferred from satellite radar interferometry. Science 282(5388):458–462. https://doi.org/10.1126/science.282.5388.458

Williams CA, Wadge G (1998) The effects of topography on magma chamber deformation models: application to Mt. Etna and radar interferometry. Geophys Res Lett 25(10):1549–1552

Wyering LD, Villeneuve MC, Wallis IC, Siratovich PA, Kennedy BM, Gravley DM, Cant JL (2014) Mechanical and physical properties of hydrothermally altered rocks, Taupo Volcanic Zone, New Zealand. J Volcanol Geotherm Res 288:76–93. https://doi.org/10.1016/j.jvolgeores.2014.10.008

Yamamoto T (2005) Eruptive history of Azuma volcano, NE Japan during last 7000 years: stratigraphy and magma-plumbing system of the Azuma-Jododaira products. J Geol Soc Japan 111:94–110 (**in Japanese with English abstract and figure caption**)

Yang XM, Davis PM, Dieterich JH (1988) Deformation from inflation of a dipping finite prolate spheroid in an elastic half-space as a model for volcanic stressing. J Geophys Res 93(B5):4249–4257. https://doi.org/10.1029/JB093iB05p04249

Yoshida K, Hasegawa A, Yoshida T (2016) Temporal variation of frictional strength in an earthquake swarm in NE Japan caused by fluid migration. J Geophys Res Solid Earth 121(8):5953–5965. https://doi.org/10.1002/2016JB013022

Yunjun Z, Amelung F, Aoki Y (2021) Imaging the hydrothermal system of Kirishima volcanic complex with L-band InSAR time series. Geophys Res Lett 48(11):1–12. https://doi.org/10.1029/2021GL092879

## Publisher's Note